ELSEVIER

Journal of Nuclear Materials 246 (1997) 17–29

journal of nuclear materials

Defocussed TEM contrast from small helium bubbles in copper

K.J. Stevens *, P.B. Johnson

Department of Physics, Victoria University of Wellington, P.O. Box 600, Wellington, New Zealand

Received 22 March 1996; accepted 3 April 1997

Abstract

The theoretical defocussed contrast of the TEM images of bubbles is computed using simulations based on the two-beam dynamical theory of electron diffraction. The bubble parameters used are chosen to be typical of the small (~ 2 nm in diameter) bubbles found in gas-bubble superlattices. Simulated images are calculated for single equilibrium bubbles, for isolated columns of equilibrium bubbles and for single overpressured bubbles in copper. The calculated images are found to depend strongly on many parameters: the depth, pressure and radius of bubbles; foil thickness; diffracting vector; excitation error; defocus level, small deviations from the Bragg angle and number of bubbles included in the column. Representative examples are presented and comparisons made with experiment. It is concluded that simulations provide a very useful framework for guiding the broad choice of imaging parameters and provide a basis for the interpretation of the complicated imaging behavior often encountered in practice. Various methods for measuring bubble radii from TEM micrographs are assessed. © 1997 Elsevier Science B.V.

1. Introduction

1.1. Gas-bubble superlattice

There have been many experimental studies based on transmission electron microscopy (TEM) of the small gas bubbles produced in metals by the ion implantation of inert gases such as helium. At low temperatures $\sim 0.2\ T_m$ (where T_m is the melting temperature of the metal) the mobility of vacancies is low and the ordering of bubbles to form a gas-bubble superlattice is a striking feature. See, for example, Refs. [1,2]. The superlattice has the same symmetry as that of the host metal. The bubbles occur at high concentrations and are of uniform size. Although approximately spherical, they are frequently faceted. See, for example, Ref. [3]. Bubble diameters are usually in the range 1 nm to 2 nm. The lattice constant (a_f) for a bubble superlattice is typically 5 to 8 nm, which is only ~ 20 times the lattice constant of the host metal; the corresponding bubble concentrations are high, $\sim 10^{25}$ m^{-3}.

Inert gas implantations are accompanied by high rates of damage in the form of the generation of host interstitial–vacancy pairs. The damage level in the implanted layer by the end of the helium implantation is estimated to exceed 10 atomic displacements per atom (dpa). The pressure of gas in the bubble cavity imposes a stress field on the surrounding matrix. For an overpressured bubble, the surrounding matrix is in radial compression and tangential tension, whereas for an empty cavity (a void) the matrix is in tangential compression and radial tension. An equilibrium bubble is one containing gas at a pressure that precisely balances the surface tension of the metal. In this case no nett stress is imposed on the matrix beyond the bubble surface. The bubbles produced at low temperature are expected to be overpressured and this has been confirmed experimentally [4,5]. For a bubble that is overpressured, bubble growth is thought to be by an athermal process such as dislocation punching [6–10].

The theories of bubble ordering leading to the formation of the gas-bubble superlattice divide into three classes according to the relative importance of the following mechanisms: (i) an elastic interaction between bubbles [11–13], (ii) the planar diffusion of host interstitial atoms [14–17] and (iii) an interaction between dislocation loops

* Corresponding author. Present address: Metallurgy Section, Materials Performance Team, Industrial Research Ltd., PO Box 31 310, Lower Hutt, New Zealand.

PII S0022-3115(97)00089-5

assumed to be punched out from the overpressured bubbles as they grow [9,18–20]. In their simplest form the dislocation-punching theories are based on the assumption that there are dislocation loops of diameter comparable to that of the bubbles retained in the metal 'wall' separating nearest-neighbor bubbles. Johnson et al. (see, for example, Ref. [1]) have argued that although the presence of discrete dislocations on this scale is unlikely, nevertheless lobes of high compression could still be expected to exist in the matrix between nearest-neighbor bubbles.

1.2. TEM imaging

The TEM imaging of very small bubbles at high concentration in the presence of high levels of gas, damage, dislocations and strain in the matrix poses particular difficulties. The high levels of defects and stress in the implanted layer results in the Kikuchi lines being either completely absent or at least poorly defined. This causes difficulty in tilting implanted specimens in the microscope to precise crystallographic orientations. In direct micrographs taken with the electron beam precisely along a principal zone in the metal, the bubble array is almost totally obscured by a widespread darkening of the field of view. (The degree of darkening appears much stronger than that observed in unimplanted crystals under similar conditions.) When inspected in detail, this obscuring image has a granular structure on a very fine scale that is suggestive of the presence in the implanted layer of small centers of strain at a concentration comparable with or higher than the concentration of the bubbles. This raises the possibility that the field darkening might arise from small dislocation loops distributed through the bubble array.

In previous work it has been found that the field of view can usually be cleared sufficiently to obtain satisfactory bubble images by tilting the specimen off-zone through 5 to 10° in an arbitrary direction. At this degree of tilt there are still many diffracted beams contributing to the bubble images. The bubbles are usually viewed in bright-field conditions. Usually, a degree of defocus is used to give bubble images which are dark against a light background. (The defocus level needed to achieve this has generally been assumed to correspond to overfocus conditions although, in previous work, this has never been rigorously tested.) These have become the standard conditions for imaging ordered bubble arrays. Under these conditions the bubble images have well-defined edges where the intensity rapidly rises to the background level and the diameter of the bubble is simply taken to be equal to the lateral extent of the image. Some justification for this procedure is provided by the theoretical analysis of TEM image formation for cavities by Rühle and Wilkens [21]. However, the accuracy of measurement of bubble diameters in a practical case remains uncertain.

Since dislocation loops between bubbles have never been imaged in TEM studies, it could be argued that such loops are not present in the bubble array. The alternative possibility is that, although present in the array, such dislocations are simply not being imaged in a recognizable form under the imaging conditions used.

1.3. This work

Much of the research in this area has been stimulated by an expectation that studies of bubble formation and bubble ordering will lead to a better understanding of microstructural development more generally. To clarify the processes underlying the growth and ordering of bubbles requires the development of a better theoretical understanding of the TEM imaging of small bubbles, especially in the complicated environment prevailing in the gas-bubble superlattice. This paper reports the results of computer simulations of bubble images for near two-beam conditions as a contribution towards providing a better theoretical basis. We concentrate on the imaging of bubbles alone, and delay reporting on the complications arising from the possible presence of dislocations, to a later study. Combinations of TEM imaging parameters are investigated which in previous work have usually been considered only in isolation. Some representative previous studies [21–28] are summarized in Table 1. The bubble sizes and spacings used in the simulations are appropriate for bubbles found in gas-bubble superlattices.

Computing and modelling limitations mean that simulations are necessarily based on highly simplified models. Further, there are a large number of adjustable imaging parameters including the foil thickness, the particular reflections excited, the excitation error (a measure of the degree of specimen tilt) and the amount of image defocus. An exhaustive investigation of all the possible combinations of imaging parameters that could be encountered in practice, lies beyond the scope of the present work. Here we investigate some selected examples in an effort to gain a better understanding of imaging behavior.

All the simulations are for bubbles in copper. The particular cases selected for detailed examination are: (i) the intensity at the center of the image, $I(0)$, of an equilibrium bubble as a function of the depth of the bubble in the foil; (ii) the intensity as a function of radial distance (i.e., the intensity profile, $I(\rho)$ vs. ρ), for the image of an equilibrium bubble for a range of bubble radii; (iii) the use of a visibility criterion as a means of determining the radius of a bubble; (iv) employing 'through-focal-series' as a method of measuring the radius of a bubble; (v) the 'in-focus' intensity at the image center, $I(0)$, for a column of equilibrium bubbles, containing two or six bubbles, as a function of the excitation error; (vi) the intensity at the image center, $I(0)$, for a column of equilibrium bubbles, containing one, three or six bubbles, as a function of the degree of defocus (at a constant excitation error); (vii) the image intensity profile, $I(\rho)$ vs. ρ, for a column of

Table 1
Representative examples of previous work

	Author, date							
	A, 1963	B, 1965	C, 1966	D, 1969	E, 1975	F, 1979	G, 1982	H, 1996
Bubbles								
Foil thickness	√	√		√	√			√
Cavity depth	√	√		√				√
Cavity radius	√	√	√	√	√		√	√
Cavity pressure	√		√	√				√
Cavity stacks						√		√
TEM								
Excitation error	√	√		√	√	√		√
Defocus level					√	√	√	√
Mathematical								
Strain included [a]	√			√				√
Solution H–W DEs	N. Int.		N. Int.	N. Int.				N. Int.
Defocus method					Fourier		Fourier	Fourier [b]
Bloch waves					√		√	
Matrix algebra		√				√		

[a] If strain is not included then the analysis is restricted to an equilibrium bubble.
[b] A Fourier method was used to defocus the beam in the $|\boldsymbol{R}| > 0$ case and numerical integration in the $|\boldsymbol{R}| = 0$ case, where $\boldsymbol{R}$ is the strain in the matrix at the bubble surface.
A: Ashby and Brown [22,23].
B: Van Landuyt et al. [24].
C: McIntyre and Brown [25].
D: Ingram [26].
E: Rühle and Wilkens [21].
F: Johnson et al. [27].
G: Foreman et al. [28].
H: This work.

equilibrium bubbles containing one, three or six bubbles, with the axis of the column in the direction of the incident electron beam (and so tilted with respect to the matrix); (viii) the image intensity profile for a bubble with a non-zero surrounding strain field (i.e., an overpressured bubble).

2. Electron diffraction theory and the simulation system

Two different formulations of the theory of electron diffraction are used in this paper. An exposition of these formulations can be found in several sources [21–29] and so are not repeated here. The first approach ignores the effects of strain altogether and uses an analytical solution for the Howie–Whelan differential equations. Numerical integration is used to defocus the analytical wave function at the exit surface of the foil.

The second approach includes the effects of a non-zero displacement field [22]. This necessitates the use of numerical integration to solve the Howie–Whelan differential equations. Here we simulate defocussed images of structures with non-zero strain fields using an approximate Fourier series approach instead of the analytical expressions of Rühle and Wilkens [21] or the numerical integration methods of Gruschel et al. [30–32]. This Fourier series approach has been used previously [28], but on structures without displacement fields.

The computer simulation and image processing system has been described previously [3]. Subsequent changes have been the upgrade of the Semper 5 software to Semper 6.3 and the replacement of the Data General MV 4000 by a Sun Sparcstation 1.

3. The construction of the displacement field

The displacement field surrounding an overpressured bubble is described by Ingram [26] and by Mindlin and Cheng [33]. The latter reference gives a displacement field for various defects, including that of a center of dilatation. Ingram models the diffraction from a void by using the displacement field of Mindlin and Cheng with a negative dilatation.

The simulations here are for a single overpressured

bubble with no associated dislocation loops. The displacement field around the bubble is taken to be spherically symmetric.

4. Results and discussion

4.1. General

Because of the large number of possible combinations of the imaging parameters, a preliminary series of simulations [34] were undertaken to explore the effects on the calculated bubble image of making broad changes in parameters such as the foil thickness, the depth of the bubble, the particular reflections excited, the excitation error and the amount of image defocus. The exploratory simulations showed that the image contrast depended strongly on most parameters. However, to make the detailed investigations tractable, the simulations were limited to a standard diffraction vector of $\boldsymbol{g} = \langle 200 \rangle$ and changes to the bubble depth and foil thickness were kept to a minimum.

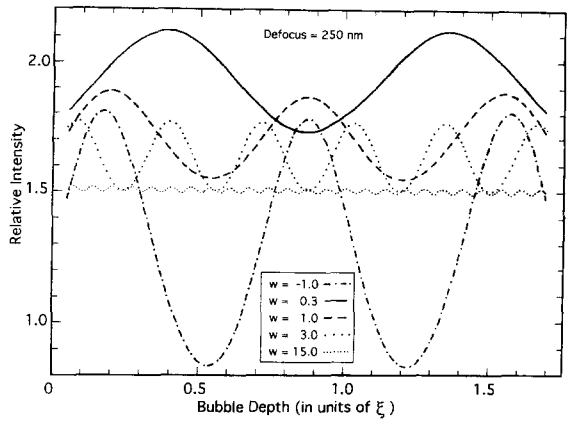

Fig. 1. Calculated intensity $I(0)$ (normalized to the background intensity) at the center of the projected image of an equilibrium bubble as a function of bubble depth, for selected values of specimen tilt as measured by the excitation error w. Bubble depths are in units of the extinction distance, ξ_g. The simulations are for a bubble radius of 1 nm in a copper foil of thickness $t = 1.750\xi_g$, with imaging parameters: underfocus = 250 nm, $\boldsymbol{g}$ = [200] and $E = 100$ keV.

4.2. Single equilibrium bubble

4.2.1. Defocussed intensity, image center

The analytical solution to the Howie–Whelan differential equations [29] has been combined with the theory of Rühle and Wilkens [21] to calculate the defocussed intensity in the image of an equilibrium helium bubble in copper. The simulation is for a degree of underfocus of 250 nm. (Experimentally, bubble arrays are often first surveyed in underfocus.) The calculated intensity at the center of the image as a function of bubble depth, is given in Fig. 1 for selected values of the excitation error, w. (The excitation error provides a measure of the degree of tilt of the specimen away from the angle that satisfies exactly the Bragg condition.)

The results show that for non-zero excitation errors, the image intensity depends to some extent on the depth of the bubble. Whereas for positive tilts the sign of the bubble contrast remains constant with depth, for the small negative tilt investigated ($w = -1.0$), at some depths the contrast is reversed. As w is increased beyond 0.3, the mean relative intensity and the variation in relative intensity with bubble depth both decrease. For the highest tilt investigated, $w = 15.0$, apart from small amplitude oscillations the relative intensity is essentially constant at 1.5 independent of the bubble depth.

4.2.2. Overfocus, radial intensity profiles

The same mathematical approach has been used to calculate intensity profiles across the image of a bubble. The intensities (normalized to the background intensity outside the bubble image) are calculated as a function of ρ, a dimensionless variable equal to the distance from the center of the image normalized to the bubble radius. The results, presented in Fig. 2 for zero tilt ($w = 0$) and two values of overfocus, show that as the size of a bubble increases, the intensity in the central region of the image becomes increasingly different from the background intensity. Although all the profiles extend with non-zero contrast beyond the ideal cut-off value of $\rho = 1$, for larger bubbles at least, the contrast beyond the bubble perimeter is small compared with that for $\rho < 1$, and tends to be oscillatory.

It is interesting that under these conditions there is no meaningful contrast for very small bubbles (bubbles with radii ~ 0.5 nm or less). For radii ~ 1 nm, and larger, better estimates of bubble radius could be made with an overfocus of 400 nm than with 800 nm. If the bubble edge is taken at the position (corresponding to the smallest radius) where the intensity has risen to within say 90% of the background intensity, the error in determining the radius of a bubble from measurements on the bubble image is estimated to be $\sim 20\%$ for a bubble of radius 1 nm. The error decreases with increasing bubble radius, falling to $\sim 5\%$ for a bubble of radius 1.5 nm.

4.2.3. Bubble radius, visibility criterion

When viewing a bubble image in a TEM micrograph by eye, the edge of the image seems well defined. The eye is sensitive to the differences in intensity between the bubble image and background, and to sharp changes in the intensity. Rühle and Wilkens [21] took both the intensity difference and the slope of the intensity profile into account in simulated measurements of the bubble radius.

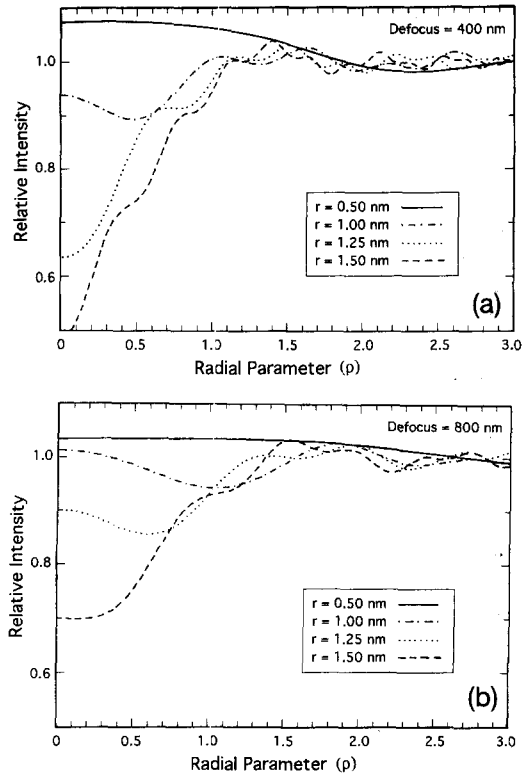

Fig. 2. Calculated intensity $I(\rho)$ as a function of radial position in the projected image of an equilibrium bubble at depth $= t/2$ where t is the foil thickness. The radial parameter, ρ, is the radial distance normalized to the bubble radius r. (Note the suppressed zero on the vertical scale). The simulations are for overfocus = 400 nm (a) and = 800 nm (b), with $w = 0$, $\boldsymbol{g} = [200]$, $t = 1.675\xi_g$ and $E = 100$ keV.

This was done by means of a visibility modulus, V, of the form

$$V \propto \left| [I(r) - I(0)] \frac{\mathrm{d}I}{\mathrm{d}r} \right|,$$

where $I(r)$ is the local image intensity, $I(0)$ is the background intensity and r is the distance from the center of the image. The radial distance, ρ, corresponding to the bubble radius, is the radial distance at which V first has a local maximum when traversing the intensity profile in the direction of increasing radius, starting at the center of the projected image.

Here, this visibility criterion is used to determine ρ as a function of bubble radius for the image of an equilibrium bubble. The range of bubble sizes covered (radii from 0.5 nm to 1.5 nm) corresponds to the range found in gas-bubble superlattices. Data have been drawn from a large set of profiles of the type represented in Fig. 2(a). The results are shown in Fig. 3. The ρ values depart significantly from the ideal value of $\rho = 1$ except at small values of the bubble radius. It is interesting that a visibility modulus of the above mathematical form gives rise to discontinuities at particular bubble radii. The simulation results suggest that the radius found using this visibility criterion (if applied uncritically) could be in error by over 60% under these imaging conditions. As discussed in Section 5, in practical cases the potential error is expected to be much less.

4.2.4. Bubble diameter, through-focal series

In an effort to reduce the uncertainties associated with other methods, an investigation has been made using experimental through-focal series as a method of determining bubble diameters. A through-focal series of projected TEM images of a particular bubble found in helium implanted copper was taken with the following imaging parameters: the electron beam directed down $\mathbf{B} = [011]$ in the matrix, $\boldsymbol{g} = [200]$, $w = 0.0$ and electron energy = 120 keV. The experimental TEM images were collected and stored in digital form. (The position of zero defocus was reckoned to be uncertain by ± 200 nm.) The '*extract*' command of the Semper image processing software allows profiles to be obtained at different angles across the digitized image (in the image plane). To minimize the effects of noise, the following procedure was adopted. The bubble image was highly magnified so that it was many pixels in lateral extent. Twenty or more separate parallel line scans were taken through the digitized image with each new line scan being displaced laterally by one pixel relative to the previous scan. The final profile was taken as an average over these line scans. Even so the final profile still contained discontinuities resulting from noise and these were sufficient to frustrate attempts to measure the bubble diameter using the criterion based on the slope of the intensity profile. For this reason the image diameter was taken to be

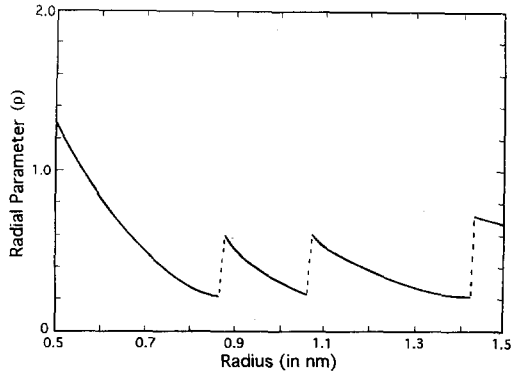

Fig. 3. Calculated radial distance, ρ, of the maximum in the visibility modulus, V, as a function of bubble radius over the range 0.5 nm to 1.5 nm, for the projected image of an equilibrium bubble at depth $= t/2$ where t is the foil thickness. As in Fig. 2(a), the simulation is for overfocus = 400 nm, $w = 0$, $\boldsymbol{g} = [200]$, $t = 1.675\xi_g$ and $E = 100$ keV.

the diameter of the first (i.e., smallest diameter) Fresnel fringe in the image.

For comparison with the experimental profiles, simulated profiles were calculated for bubbles of different sizes at the various values of defocus used experimentally. The foil thickness and the bubble depth in the simulations were $1.675\xi_g$ and $1.675\xi_g/2$, respectively. The diameter of the actual bubble was then determined by comparing the experimental profiles with the simulated profiles. The best fit with experiment was obtained for simulations based on a bubble diameter of (2.5 ± 0.1) nm. The results for these simulations are shown in Fig. 4. No detailed study has been made of the effects of varying the bubble depth or the foil thickness in the simulations.

4.3. Column of equilibrium bubbles

4.3.1. In-focus, central intensity vs. tilt

The gas-bubble superlattice in copper typically comprises small ($\sim$ 1 nm radius) helium bubbles arranged on a superlattice of lattice constant $\sim$ 7 nm. When viewed along a principal crystallographic direction, the bubbles can be regarded as being arranged in columnar stacks with the column axes along the viewing direction. In the case of the [011] direction ($\langle 011 \rangle$ are the close-packed directions in an fcc lattice), the bubbles in a given column will be separated by approximately 5 nm. Here, we investigate the imaging of such stacks by calculating the projected images for a single column of equilibrium bubbles of bubble radius 1 nm, and inter-bubble spacing 5 nm along the [011] column axis.

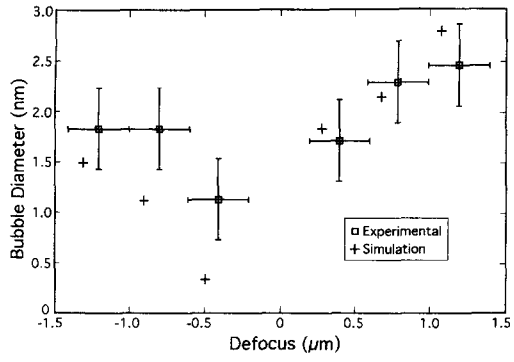

Fig. 4. The experimentally determined diameter of the first Fresnel fringe, as a function of the degree of defocus, for the projected TEM image of a particular bubble found in helium implanted copper. The parameters used in the microscope examination were $\mathbf{B} = [011]$, $\boldsymbol{g} = [200]$, $w = 0$ and $E = 120$ keV. Simulated intensity profiles, $I(\rho)$ vs. ρ, were calculated for different bubble sizes and different values of defocus (for a foil thickness of $t = 1.675\xi_g$ and a bubble depth $= t/2$). A comparison of these theoretical profiles with the experimental profiles found in through-focal series, allowed an estimate to be made of the diameter of the bubble. The best match was obtained for a bubble diameter of 2.5 nm. The results of the simulations for this bubble diameter are shown in the figure (+).

Patterns of projected bubble images in bright field micrographs taken with the electron beam directed down [011] in (011) grains, show that the lateral ordering of the helium gas-bubble superlattice in copper seldom extends over a region greater than a square area corresponding to about six gas bubbles per side. The ordering along the [011] normal to the grain surface is thought to be similarly limited in extent and so in the simulations the maximum number of bubbles included in the column has been restricted to six. (The nature of the ordering of bubbles in a plane oblique to the surface has been investigated in a recent experimental study [35].) To space the bubbles regularly, the foil thickness in a simulation must be increased as the number of bubbles is increased. A column of six bubbles spaced at 5 nm in copper gives a foil thickness of about one extinction distance, only. The simulations relate then to the experimental situation in which a bubble column is located near the thin edge of the foil.

Micrographs of superlattices are usually taken with the beam tilted away from two-beam conditions to remove obscuring strain images. The 'in-focus' intensity at the center of the image, $I(0)$, has been calculated as a function of specimen tilt (as measured by the excitation error w) for columns containing from one to six bubbles. To make the simulations tractable, the column axis has been allowed to move relative to the matrix during the tilt so as to always keep the column axis parallel to the incident electron beam. The results for columns of two and six bubbles are shown in Fig. 5(a), (b), respectively. Such curves are known as bright field rocking curves. The curves exhibit large dips in the intensity (around $w = -7$ and $w = +7$) of a magnitude roughly proportional to the number of bubbles. Johnson et al. [27] attributed the origin of these dips to transmitted electrons which are multiply diffracted, so as to be out of phase with the electrons that are directly transmitted. The resulting cancellation leads to the dips in intensity.

4.3.2. Central intensity vs. defocus

Experimentally it has been found that with the superlattice tilted away from two-beam conditions, there are degrees of overfocus where the bubbles appear dark against a light background and degrees of underfocus where the bubbles appear white against a dark background. This is the expected imaging behavior. However, there are also degrees of defocus where the imaging is less clearly defined. To clarify the imaging behavior, the intensity $I(0)$ at the center of the image of a bubble column has been calculated as a function of defocus and the number of bubbles in the column, for the particular excitation error $w = 15$.

The results, given in Fig. 6, show that the defocus curves have broad minima in overfocus (defocus values of 200 nm to 300 nm), and broad maxima in underfocus

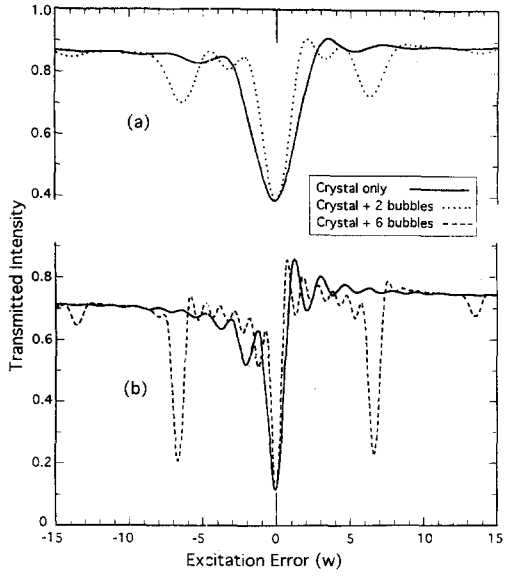

Fig. 5. Calculated 'in-focus' intensity $I(0)$ at the center of the projected image of a column of regularly spaced, 1 nm radius, equilibrium bubbles, as a function of specimen tilt measured in terms of the excitation error, w. The simulation is for near two-beam conditions with $\boldsymbol{g} = [200]$. Curve (a) is for a column of two bubbles and (b) is for six bubbles. (Such curves are referred to as bright-field rocking curves.)

(defocus values of -100 nm to -400 nm). This behavior is consistent with the experimental observations. The profiles also show that there are values of overfocus where the intensity in the center of the image of the column exhibits reverse contrast (i.e., the transmitted intensity is above background in overfocus). This is the case, for example, for overfocus values of around 150 nm. Similarly, in underfocus the image of the column can exhibit reverse contrast and appear dark (for example, at values of defocus less than -400 nm).

4.3.3. Overfocus, radial intensity profile vs. No. of bubbles

Simulations have been performed for a column of bubbles, to investigate the dependence of the radial intensity profile on the number of bubbles in the stack. The results of the previous section indicate that for the imaging conditions used there, a minimum in the central intensity $I(0)$ occurs for an overfocus of 200 nm. Further, as can be seen from Fig. 6, for a bubble column containing more than one bubble an overfocus of 200 nm is still sufficiently close to the minimum that the central intensity $I(0)$ remains appreciably less than unity. For these reasons an overfocus of 200 nm is used in the present simulations. The other imaging parameters are set to the same values as those used in the calculations summarized in Fig. 6. The calculated radial profiles for one, three and six bubbles are shown in Fig. 7.

The curve for one bubble has a large central minimum in the intensity followed by smaller oscillations as ρ increases. This predicted behavior is plausible when compared with experiment. For more than one bubble in the column, the intensity profiles exhibit pronounced oscillations in intensity near and beyond the perimeter of the projection of the bubble column on the image plane. The peaks and the dips in the profiles occur in similar positions for differing numbers of bubbles in the stack. However, the amplitudes of the oscillations increase as the number of

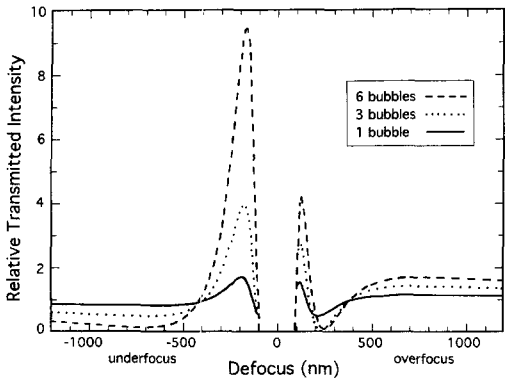

Fig. 6. Calculated intensity $I(0)$ at the center of the projected image of a column of regularly spaced, 1 nm radius, equilibrium bubbles, as a function of the degree of defocus. The simulation is for near two-beam conditions with $\boldsymbol{g} = [200]$ and $w = 15.0$. Curves are given for a single bubble and columns of 3 and 6 bubbles. The region around zero defocus has been omitted because of the rapid fluctuations in calculated intensity in this region. (Experimentally, this region is avoided because there is little bubble contrast for small values of defocus.)

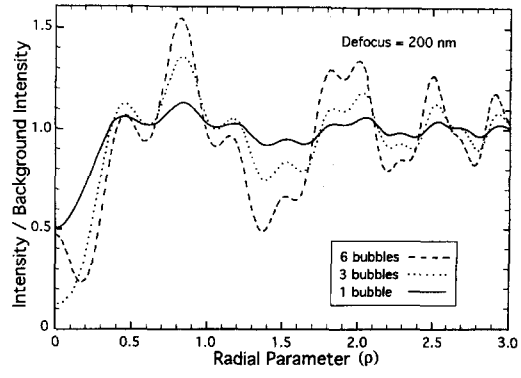

Fig. 7. Calculated intensity $I(\rho)$ in the projected image of a column of regularly spaced equilibrium bubbles, as a function of radial position. The radial parameter, ρ, is the radial distance normalized to the bubble radius, r. The simulation is for $\boldsymbol{g} = [200]$, $w = 15.0$ and overfocus = 200 nm. (An overfocus of 200 nm corresponds to the minimum in the intensity at the center of the image for a single bubble and is close to the overfocus required to give an intensity minimum for columns involving more than one bubble — see Fig. 6.) Curves are given for a single bubble and columns of three and six bubbles.

bubbles in the stack increases. Similar dependencies were found in simulations performed both for other defocus levels and for $w = 0$. Experimentally, large oscillations of this type have not been identified and it could be tempting to interpret this as demonstrating that the ordering along the direction of the electron beam must be limited to at most a few bubbles only. However, as discussed further in Section 5, the differences between the practical case and the idealized model used in the simulations means that drawing such a conclusion could be misleading.

4.4. Single overpressured bubble

The bubble overpressure is the amount by which the pressure inside the bubble exceeds the equilibrium pressure. An overpressured bubble sets up a strain field in the surrounding matrix and so has imaging characteristics different from those of a bubble at equilibrium pressure. This non-zero strain field necessitates the use of numerical integration to solve the Howie–Whelan differential equations. The question arises as to what degree of bubble overpressure should be used in the simulations, given that the overpressure needed for bubble growth by dislocation punching is not known for a bubble in the environment of a gas-bubble superlattice. There are two major sources of uncertainty. (i) The overpressure required for dislocation punching is expected to be directly proportional to the shear modulus of the metal — the microscopic (as opposed to the macroscopic) shear modulus is simply not known (although bounds can be placed on it). (ii) Equally, the effects of backpressure, from the presence of neighboring bubbles, on bubble growth by dislocation punching are not known at a detailed level although Dubinko et al. [18] have done some modelling of this situation for ordered arrays.

Cochrane and Goodhew [36] investigated the TEM contrast of an isolated bubble as a function of bubble overpressure and found that the images exhibited strain contrast for degrees of overpressure exceeding a threshold between 0.50 to 0.75 GPa. The emphasis in their work is on small values of overpressure. Given the uncertainties in the degree of overpressure in the superlattice case, a high value of overpressure (10 GPa) is used here both to model as closely as possible the practical case and to enable the effects of a large displacement field to be gauged.

Many simulations have been performed for overpressured bubbles with a variety of imaging parameters [34]. A common feature of the simulated images is a departure from the cylindrical symmetry that is found in the images of equilibrium bubbles. As an example, the projected image of a single isolated overpressured bubble, calculated for a defocus of ~ -340 nm (underfocus), is shown in Fig. 8. The contrast inside the bubble radius is dominated by thickness contrast. The large displacement field gives rise to strain contrast in the form of asymmetrical black and white lobes which extend significantly outside the perimeter of the bubble.

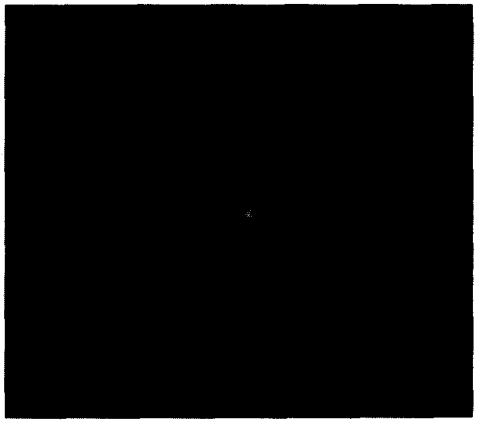

Fig. 8. A simulated projected image of a single isolated overpressured bubble at a defocus of ~ -340 nm (underfocus). The bubble overpressure (the amount by which the pressure inside the bubble exceeds the equilibrium pressure) is 10 GPa. The other parameters in the simulation are $\boldsymbol{g} = [200]$, $w = 0.0$, $E = 100$ keV, foil thickness $t = 1.675\xi_g$ and bubble depth $= t/2$. (It is found that overpressure gives rise to a departure from cylindrical symmetry in the image. Note the black and white lobes which extend well beyond the bubble perimeter.)

5. Discussion

5.1. General

As discussed below, it is clear that the simulations provide a very useful framework for guiding the broad choice of imaging parameters and provide a basis for the interpretation of the complicated imaging behavior that is often encountered in practice. At a detailed level, however, there are difficulties in assessing how well the simulations model the imaging of bubbles in the complex environment of the bubble superlattice. Similarly, it is difficult to assess the accuracy of the different TEM based methods proposed for measuring bubble radii. The particular problem here is the absence of any alternative method for measuring bubble radius that could provide an independent comparison.

The results obtained here for bubble columns are consistent in broad outline with those of Johnson et al. [27]. It is not possible, however, to make direct comparisons because of the differences in the situations modelled in the two cases. Their results were for a fixed foil thickness of $4\xi_g$ and for a single cavity diameter of $0.1\xi_g$. Hence, compared with the present work, they examined larger cavities in much thicker foils. Also, the emphasis in their work was on cavities produced by 200 keV electron irradiation of metal halides such as calcium fluoride, rather than helium implanted metals.

In comparing the results of simulations with experiment, a factor to consider is that when imaging bubbles in the microscope the imaging parameters are normally adjusted to give the clearest possible bubble images. Although oscillations of the type predicted by some of the simulations are clearly observed in practice [34], it has only been for isolated bubbles that are larger than those found in the superlattice. In previous work, it is likely that if oscillations had been present, the microscope parameters would have been readjusted to minimize them. (The simulations show that even small changes in imaging conditions can have a large effect on the appearance of the images obtained.) As a result, it is difficult in some cases to make meaningful comparisons with earlier experiments.

5.2. Single equilibrium bubble

5.2.1. Defocussed intensity, image center

Under the underfocus imaging conditions of Fig. 1, for positive tilts greater than $w = 1.0$, the predicted variation in intensity with depth is relatively small. Such small variations may not be noticed under experimental conditions. Except for the case $w = -1.0$, the image contrast is light against a darker background (i.e., intensity/background > 1) at all bubble depths. This behavior is in accord with the common 'rule of thumb' that bubbles appear dark relative to background in overfocus and light relative to background in underfocus.

It is interesting that there are imaging conditions where the image contrast oscillates from one type to the other as the depth of the bubble is changed. This is the case here for $w = -1.0$, where the contrast reverses for narrow depth regions near $0.5\xi_g$ and $1.2\xi_g$. This could explain the common experimental observation that under some imaging conditions there are images that seem to be from bubbles but which have contrast opposite to that of the majority of the bubbles. This type of simulation shows that the criterion of 'light bubble images against a dark background' cannot be taken as an unambiguous indicator of underfocus imaging conditions.

For high tilt values, e.g., $w \sim 15.0$, the relative intensity in the image center is essentially constant independent of the bubble depth. This suggests that experimentally, in underfocus, tilt values around 15 could be used to give all the bubbles in the array a similar appearance irrespective of bubble depth.

5.2.2. Overfocus, radial intensity profiles

The images of bubbles with radii below ~ 1 nm have very little contrast under the imaging conditions of Fig. 2. For bubble radii of ~ 1 nm and greater, the contrast is that expected for overfocus conditions with the bubbles appearing dark relative to background. Within the range of radii investigated, the larger the bubble the better the contrast. This predicted behavior could explain a recent experimental observation relating to helium bubble structures in vanadium [37]. In that work the bubbles in a wedge-shaped specimen, which covered a range of different thicknesses, were imaged in the same micrograph (Fig. 2, Ref. [37]) and hence with the same microscope imaging parameters. The electron beam was directed down $\langle 110 \rangle$ in the matrix, and the bubbles were imaged in overfocus contrast. (The other imaging parameters were not noted.) It was inferred that in the thicker regions of the specimen there were small bubbles near the surface of the specimen with large bubbles lying below them. However, under the particular imaging conditions used, the imaging was dominated by the largest cavities in the thinned section to such an extent that the small bubbles lying closer to the surface were not discernible.

To determine the radius of a bubble from the lateral extent of a TEM image, some criterion is needed to select the part of the image that is to be taken as the outer boundary of the bubble. The results of Fig. 2(a) suggest that the perimeter of the bubble could be identified with the position on the image of greatest radial distance where some decrease from the background intensity can be discerned and where the intensity continues to decrease with decreasing radius. One possibility is to associate the bubble perimeter with the position where the intensity has fallen to some fixed fraction of the background intensity. The fixed fraction might be taken as 90%, for example. (The errors in determining bubble radii for this particular fraction have been examined in Section 4.2.2.)

Another possible approach for locating the boundary of the bubble on the bubble image would be to consider intensity differences from background rather than absolute intensities. First, the background intensity would be subtracted from all the calculated intensities. Then, provided the intensity difference from background at the image center $(I_o - I_b)$ is not small, the intensity differences from background would all be normalized to the intensity difference $(I_o - I_b)$. The edge of the bubble could then be taken to be the position where the normalized intensity was some chosen fraction. The uncertainties associated with such a procedure have not been investigated here, but provided $(I_o - I_b)$ is not small, they could be less than those associated with the method based on simply taking a fixed fraction of the background intensity.

The results obtained here for an overfocus of 400 nm raise a further possibility for measuring bubble radii. The calculations show that the intensity at the center of the bubble image is a monotonically decreasing function of the bubble radius. This suggests that the intensity at the center of the bubble image, normalized to the background intensity, could be used to provide a *relative* measure of bubble radius independent of the apparent lateral extent of the bubble image. This relative scale could be calibrated to give absolute estimates of bubble radii by using the method based on through-focal series (Section 4.2.2) to determine the radius of a few selected bubbles to act as standards. Such a procedure has the attraction that the measurement

of central intensities can easily be automated using standard image processing techniques whereas the measurements based on through-focal series are laborious and not suited to measuring large numbers of bubbles. (Large bubble numbers are needed if representative bubble volume fractions are to be determined, for example.)

5.2.3. Bubble radius, visibility criterion

For the profiles of Fig. 2, using the visibility criterion defined in Section 4.2.3 leads to bubble radii that depart significantly from the ideal value of $\rho = 1$. Except for the smallest bubbles the predicted values of ρ are generally too small. Further, Fig. 3 exhibits discontinuities in ρ at particular values of r. This results from an instability in determining the bubble edge using the visibility criterion — at certain radii a small change in bubble radius can flip the position of maximum V from one intensity oscillation to the next (at larger ρ) giving rise to a discontinuity in the apparent bubble radius.

In practice, a number of factors can be identified, such as those listed in Section 5.3.3., which are likely to damp out the oscillations and lead to more realistic values of bubble radii being obtained. Perhaps the most important factor is that discussed in Section 5.1, namely that in the practical case imaging conditions, although selected within broad parameters, are adjusted finally to give images with well-defined edges free from oscillations and the largest possible lateral extent. For these reasons the errors resulting from using the visibility criterion in practice are probably much less than those suggested by the simulations. What the simulations do show, however, is that the criterion must be applied critically if large errors are to be avoided.

5.2.4. Bubble diameter, through-focal series

The agreement obtained between experimental through-focal series and simulations in which the bubble radius is treated as an adjustable parameter provide perhaps the best confirmation of the validity of the theoretical basis of the simulations. The results suggest that this is the most accurate method for measuring bubble radii. However, the method is complicated and likely to be limited to measuring a few bubbles only, in practice. As outlined in Section 5.2.2, this procedure based on through-focal series might best be used to provide standards for calibrating those methods which, although they give relative bubble radii only, are easier to apply to large numbers of bubbles.

5.3. Column of equilibrium bubbles

5.3.1. In-focus, central intensity vs. tilt

The effect of tilting the crystal containing a column of bubbles, away from two-beam conditions, through an angular range of approximately -1.5 mrad to $+1.5$ mrad, is shown in Fig. 5. The rocking curves obtained show that there is little contrast between bubbles and matrix for in-focus conditions and values of w near zero. Away from $w = 0$, the effect of bubbles is to introduce additional oscillations into the curves. A relatively high value of tilt, $w = 15$, is chosen for the other simulations on bubble columns. This avoids the oscillations found at low values of w and matches more closely the experimental situation where, because of the high levels of damage in the crystal matrix, it has proved difficult to locate strong two-beam conditions precisely. Also, although detailed studies have not yet been done, there is some evidence from simulations to suggest that for the higher tilt values the bubble images have a reduced sensitivity, for a broader range of combinations of the other imaging parameters, to changes in both bubble depth and foil thickness.

In the simulations, the bubble column is allowed to move relative to the matrix so as to maintain the column axis along the electron beam direction as the specimen is tilted. The question arises as to the effects of this approximation. The Bragg angle for exciting a {200} reflection in copper with 100 keV electrons, is 10.3 mrad. The extinction distance for a {200} reflection is 33.4 nm. The excitation error of $w = 15$ corresponds then, to an extra tilt away from the Bragg angle of 1.5 mrad. Consider the particular reflection with reciprocal lattice vector, $\boldsymbol{g} = [200]$, excited with the electron beam directed down $\mathbf{B} = [011]$ in the untilted specimen. To obtain an excitation error of $w = 15$, requires a tilt of 11.8 mrad from this flat-foil condition with $\boldsymbol{g} = [02\bar{2}]$ as rotation axis. If the tilt is solely about $[02\bar{2}]$, the bubble column will then be inclined at an angle of 11.8 mrad with respect to the electron beam. Suppose that to reduce the intensity of the other matrix reflections (to obtain near two-beam conditions) the crystal is now tilted further, but with $\boldsymbol{g} = [200]$ as rotation axis. In practice a rotation of a few mrad should be sufficient for this second tilt. However, to estimate the maximum likely effect suppose this second tilt is made the same as the first, namely 11.8 mrad. The nett result is a total tilt of approximately 17 mrad away from the electron beam in a direction at 45° to $\boldsymbol{g} = [200]$. At this orientation, for a bubble column containing six bubbles, an electron that passes directly through the center of the top bubble in the column (and is not subsequently scattered) will pass approximately 0.6 nm away from the center of the last bubble in the column. It is estimated that overall, the approximation will introduce an error of less than 10% into the apparent bubble diameter and in broad terms will have little effect on the imaging behavior predicted by the simulations.

5.3.2. Central intensity vs. defocus

The simulations summarized in Fig. 6 establish several further important points. Irrespective of the number of bubbles, good contrast can be obtained in both overfocus and underfocus. This is consistent with what has been found experimentally. A suitable measure of the contrast in underfocus is the ratio of the transmitted intensity at the

bubble center to the background intensity at positions well away from the bubble. In Fig. 6 the background intensity is unity so the contrast in underfocus is simply $I(0)$. However, for degrees of overfocus that give dark bubble images against a light background (e.g., overfocus levels around 200 nm to 300 nm in Fig. 6) we take the contrast to be the *inverse* of this ratio, namely, the *reciprocal* of $I(0)$. In terms of these definitions the contrast obtainable in underfocus is similar to that obtainable in overfocus. Experimentally, overfocus conditions have generally been preferred. For overfocus, the definition and visibility of the bubble images in the microscope appear to be superior, photographic exposures are less critical and more detail can be seen in the micrographs. These features are consistent with the results shown in Fig. 6. The simulations show that for overfocus, the background brightness can be increased to provide more detailed images from the matrix surrounding the bubbles without saturating the bubble images themselves.

The optimum degree of overfocus — the level of overfocus that gives the best contrast — depends to some (small) extent on the number of bubbles in the column. The contrast at the optimum overfocus increases as the number of bubbles in the column increases. This predicted behavior is consistent with the excellent overfocus contrast that can be obtained in practice from ordered bubble arrays — see, for example, the typical micrographs for copper and for vanadium given in fig. 1 of Ref. [1], and fig. 1 of Ref. [38], respectively. Further, for a given number of bubbles in the column the contrast is not very sensitive to changes in overfocus over quite a broad range around the optimum. Finally, if the sizes of bubbles in the column vary, the results of Section 4.2.2 suggest that the imaging will be dominated by the largest bubble in the column. These results too, are consistent with experiment.

5.3.3. Overfocus, radial intensity profile vs. No. of bubbles

The simulations indicate that as the number of bubbles in the column is increased, the amplitude of oscillations near and beyond the perimeter of the image increase to a level comparable with the levels near the image center. Experimentally, such oscillations have not been identified in the images of superlattice bubbles. We speculate that in practice the oscillations may be damped out by factors such as the beam divergence, coherence effects, bubble overpressure, bubble ordering and the close proximity of neighboring bubbles (see Section 5.4), and imperfections in the bubble ordering. The latter, for example, are known to strongly affect electron diffraction patterns taken from gas-bubble superlattices in copper and other metals. The patterns often contain bubble reflections whose indices are disallowed under the normal selection rules for the lattice. The presence of these disallowed reflections has been explained in terms of imperfections in the bubble ordering in the form of small random displacements of bubbles from ideal lattice sites. Such displacements could be expected to damp out, to some degree at least, the oscillations predicted from simulations.

5.4. Single overpressured bubble

The main effects of bubble overpressure are to cause a loss of cylindrical symmetry in the simulated images and, under some conditions, to push the image contrast out beyond the actual boundary of the bubble. Under near two-beam conditions, in the plane of the image the intensity pattern is symmetric about the $\boldsymbol{g}$-vector of the excited matrix reflection. In the work of Cochrane and Goodhew [36] the emphasis is on small degrees of overpressure, in the region below 1 GPa. The simulations here are based on 10 GPa — a relatively high value of overpressure. Where overlap is expected, the results of the two studies broadly agree.

There are many factors not included in the calculations which might influence bubble imaging. For example, in practice the environment of any given bubble will be complicated by the presence of neighboring bubbles (and hence on the degree of bubble ordering), and by the high levels of gas, damage and lateral stress in the implanted layer [1]. In the simulations the strain field around the bubble has been taken to be spherically symmetric. However, as outlined in Section 1, the strain is likely to depend strongly on crystallographic direction with lobes of high compression along the dense-packed $\langle 110 \rangle$ directions. The bubble concentrations in the superlattice are so high (10^{25} per m^{-3}) that extended images of the type shown in Fig. 8 would extend laterally over the images of neighboring bubbles. Factors such as these could be expected to strongly influence the images obtained in practice, and provide a ready explanation of why extended images of this type have not been observed experimentally for bubbles in the superlattice. If the implantation temperature and helium dose are altered so that larger bubbles are formed in lower concentrations, the bubble images obtained experimentally are of the extended type predicted by the simulations [34]. In this case the metal in the implanted layer has a higher degree of crystalline perfection (as judged from the clarity of the Kikuchi lines in diffraction patterns) than in the superlattice case.

6. Conclusion

Although necessarily based on highly simplified models, the simulations provide a valuable framework within which to understand the TEM imaging of the small bubbles typically found in gas-bubble superlattices. Simulations show that in general bubble images are strongly affected by many parameters — foil thickness, depth of the bubble, bubble radius, diffracting vector, excitation error, bubble pressure, defocus level and for a column of bubbles, the number of bubbles in the column. However, for equilibrium bubbles, particular imaging conditions have

been identified for which the imaging is robust, giving high contrast images that are relatively insensitive to small changes in the main imaging parameters.

These imaging conditions, which can be summarized as near two-beam conditions with an excitation error $w \sim 15$ and moderate levels of overfocus, are probably close to those that have been arrived at empirically in experimental studies of the overpressured bubbles found in bubble lattices. (The imaging parameters used in the experimental studies are known only very approximately, mainly because of the difficulties in precisely orienting and imaging specimens that contain high levels of gas, defects and stress.) Predictions based on simulations for these particular imaging conditions show good agreement with experiment. The main results for these conditions, supported by experiment, include: (i) the larger the bubble the greater the image contrast; (ii) the larger the number of bubbles contained in a bubble column, the greater the image contrast; (iii) for a given number of bubbles in the column the contrast is not very sensitive to changes in overfocus over a quite a broad range around the optimum; (iv) if bubble sizes vary down the column the imaging is likely to be dominated by the largest bubble. These and other results clarify some previously puzzling aspects of bubble imaging.

Other, more general results, include (i) the 'conventional wisdom' that bubble images are always dark (below background intensity) in overfocus and light in underfocus, does not always apply; (ii) comparisons between a through-focal series of bright-field micrographs and simulated intensity profiles, although laborious, provide the best means of measuring the radius of a single isolated bubble; (iii) overfocus imaging conditions have been identified where the intensity at the center of the bubble image relative to background changes monotonically with bubble radius (a result that raises the possibility that a relative scale for measuring bubble radius might be based simply on measuring central intensities); (iv) underfocus imaging conditions have been identified where the relative intensity in the image center (for identical bubbles) is essentially constant independent of the bubble depth (thereby providing a possible method for identifying the depth dependent features of bubble imaging).

Acknowledgements

We thank T.T. Young, D. Housden, R.W. Thomson, and K.E. Reader of Victoria University of Wellington for their assistance. It is also a pleasure to acknowledge valuable contributions from Dr D. Cockayne and Dr Zou Jin of the Electron Microscope Unit, Sydney University, Dr C. Cook and Dr P.W. Gilberd of Victoria University of Wellington, Dr D.J. Mazey formerly of Harwell Laboratory, Oxfordshire, UK and Dr N. Zaluzec, Argonne National Laboratory, IL, USA.

References

[1] P.B. Johnson, in: Fundamental Aspects of Inert Gases in Solids, eds. J.H. Evans and S.E. Donnelly (Plenum, New York, 1991) p. 167.
[2] P.B. Johnson, D.J. Mazey, J. Nucl. Mater. 218 (1995) 273.
[3] P.B. Johnson, K.J. Stevens, R.W. Thomson, Nucl. Instrum. Methods B62 (1991) 218.
[4] S.E. Donnelly, Radiat. Eff. 90 (1985) 1.
[5] J.H. Evans, D.J. Mazey, J. Nucl. Mater. 132 (1986) 176.
[6] J.H. Evans, J. Nucl. Mater. 68 (1977) 129.
[7] J.H. Evans, J. Nucl. Mater. 76&77 (1978) 228.
[8] J.H. Evans, J. Nucl. Mater. 79 (1978) 241.
[9] P.B. Johnson, 4th Ann. Solid State Phys. Mtg Aust./ NZ Inst. Phys. 1980, Phys. Rpt 1/82, Victoria University of Wellington, Wellington, 1982.
[10] P.B. Johnson, W.R. Jones, J. Nucl. Mater. 120 (1984) 125.
[11] K. Malen, R. Bullough, in: Proc. Conf. on Voids Formed by Irradation of Reactor Materials, eds. S.F. Pugh, M.H. Loretto, D.I.R. Norris (British Nuclear Energy Society, AERE Harwell, 1971) p. 109.
[12] A.M. Stoneham, in: in: Proc. Harwell Consultants Symposium on the Physics of Irradiation Produced Voids, ed. R.S. Nelson, AERE Report R-7934, 1974, p. 319.
[13] A.G. Khachaturyan, V.M. Airapetyan, Phys Status Solidi (a)26 (1974) 61.
[14] J.H. Evans, Mater. Sci. Forum 15–18 (1987) 869.
[15] C.H. Woo, W. Frank, Mater. Sci. Forum 15–18 (1987) 875.
[16] J.H. Evans, in: Encyclopedia of Materials Science and Engineering, Suppl. Vol. 1, ed. R.W. Cahn (Pergamon, Oxford, 1988) p. 547.
[17] J.H. Evans, in: Proc. of NATO Advanced Study Institute on Patterns, Defects and Instabilities, Cargese, Corsica, Sept. 1989, eds. D. Walgraef and N.M. Ghoniem (Kluwer Academic, Dordrecht, 1990) p. 347.
[18] V.I. Dubinko, V.V. Slezov, A.V. Tur, V.V. Yanosky, Radiat. Eff. 100 (1986) 85.
[19] W.G. Wolfer, Philos. Mag. A59 (1986) 87.
[20] P.B. Johnson, A.L. Malcolm, D.J. Mazey, Nature 329 (1987) 316.
[21] M. Rühle, M. Wilkins, Cryst. Lattice Def. 6 (1975) 129.
[22] M.F. Ashby, L.M. Brown, Philos. Mag. 8 (1963) 1083.
[23] M.F. Ashby, L.M. Brown, Philos. Mag. 8 (1963) 1649.
[24] J. van Landuyt, R. Gevers, S. Amelinckx, Phys. Status Solidi 10 (1965) 319.
[25] K.G. McIntyre, L.M. Brown, J. Phys. (Paris) C3 (1966) 178.
[26] J. Ingram, J. Appl. Phys. 40 (1970) 5030.
[27] E. Johnson, E. Kynde, L.T. Chadderton, J. Microscopy 116 (1979) 15.
[28] A.J.E. Foreman, H.S. von Harrach, D.K. Saldin, Philos. Mag. A45 (1982) 625.
[29] P.B. Hirsch, A. Howie, R.B. Nicholson, D.W. Pashley, M.J. Whelan, Electron Microscopy of Thin Crystals (Krieger, Huntington, NY, 1977).
[30] W.J. Gruschel, A. Laupheimer, M. Wilkens, Proc. 10th Int. Congr. on Electron Microscopy, Hamburg, Vol. 1, 1982, p. 97.
[31] W.J. Gruschel, Comput. Phys. Commun. 16 (1979) 175.
[32] W.J. Gruschel, M. Wilkens, Phys. Status Solidi (a)89 (1985) 467.
[33] R. Mindlin, D. Cheng, J. Appl. Phys. 21 (1950) 926.

[34] K.J. Stevens, PhD thesis, Victoria University of Wellington (1993).
[35] P.B. Johnson, K.L. Reader, R.W. Thomson, J. Nucl. Mater. 231 (1996) 92.
[36] B. Cochrane, P.J. Goodhew, Phys. Status Solidi (a)77 (1983) 269.
[37] P.B. Johnson, P.W. Gilberd, Proc. 10th Int. Ion Beam Modifications of Materials Conf. 1996, IBMM-96, Albuquerque, Nucl. Instrum. Methods, in press.
[38] P.B. Johnson, D.J. Mazey, J. Nucl. Mater. 127 (1985) 30.